Advances in Applied Mathematics and Mechanics
Adv. Appl. Math. Mech., Vol. **4**, No. 6, pp. 685-702

DOI: 10.4208/aamm.12-12S01
December 2012

A Moving Mesh Method for Kinetic/Hydrodynamic Coupling

Zhicheng Hu and Heyu Wang*

Department of Mathematics, Zhejiang University, Hangzhou 310027, Zhejiang, China

Received 21 February 2012; Accepted (in revised version) 31 May 2012

Available online 9 November 2012

Abstract. This paper deals with the application of a moving mesh method for kinetic/hydrodynamic coupling model in two dimensions. With some criteria, the domain is dynamically decomposed into three parts: kinetic regions where fluids are far from equilibrium, hydrodynamic regions where fluids are near thermodynamical equilibrium and buffer regions which are used as a smooth transition. The Boltzmann-BGK equation is solved in kinetic regions, while Euler equations in hydrodynamic regions and both equations in buffer regions. By a well defined monitor function, our moving mesh method smoothly concentrate the mesh grids to the regions containing rapid variation of the solutions. In each moving mesh step, the solutions are conservatively updated to the new mesh and the cut-off function is rebuilt first to consist with the region decomposition after the mesh motion. In such a framework, the evolution of the hybrid model and the moving mesh procedure can be implemented independently, therefore keep the advantages of both approaches. Numerical examples are presented to demonstrate the efficiency of the method.

AMS subject classifications: 65M50, 76P05

Key words: Moving mesh method, kinetic/hydrodynamic coupling, the Boltzmann-BGK equation.

1 Introduction

Hydrodynamic equations such as the Navier-Stokes or the Euler equations have achieved successful applications in many areas of fluid dynamics, while there are cases that this hydrodynamic equations do not provide a satisfactory description of the physical system. Then we have to use a kinetic description by the Boltzmann equation or a simplified version of it, i.e., the Boltzmann-BGK equation. However, even nowadays the numerical solution for such microscopic models is too expensive

*Corresponding author.
URL: `http://mypage.zju.edu.cn/wangheyu`
Email: huzhicheng@zju.edu.cn (Z. Hu), wangheyu@zju.edu.cn (H. Wang)

to be solved. In most cases, we are primarily concerned about the macroscopic phenomena of the problems rather than the microscopic state which need to be solved through the microscopic model and the hydrodynamic equations can provide a sufficiently accurate description of the problems only except in very local domain where the hydrodynamic equations breakdown, such as shock wave and boundary layers. In this situations, a coupled method of the kinetic/hydrodynamic model can be expected more efficient than the whole microscopic models and still provide the correct representation of the physical phenomena. In the last few years many investigations have been achieved in this direction, such as the coupling of different models and different implementation techniques (e.g., [1–6]). Our purpose of this paper is to study a moving mesh adaptive method for the kinetic/hydrodynamic coupling model.

This paper is a further study of the kinetic/hydrodynamic coupling model introduced in [2] on 2-dimensional domain. The Boltzmann-BGK equation is used as kinetic model on kinetic regions and the Euler equations as hydrodynamic model on hydrodynamic regions respectively. We use Fig. 1 to illustrate the decomposition of the domain. Since the two regions are connected by some fixed-width buffer zones and both of the kinetic and hydrodynamic models are solved on not only their own regions but also the buffer zones, the solutions are combined with both ingredients through a cut-off function. As presented in [1,2], the use of the buffer zones and the cut-off function makes the coupling model can be solved quite smoothly without any interface condition. When the time evolutions, the kinetic regions are automatically generated based on some equilibrium criteria, which indicate the deviation from the current microscopic state to thermodynamical equilibrium if microscopic data are available, or if not, the breakdown of the hydrodynamic model. With this moving zones technique, the kinetic zones can be chosen as small as possible to speedup numerical simulations while preserve the accuracy of the physical phenomena.

Because the solution of the kinetic/hydrodynamic coupling model have large variations over some local domain, it is benefit to use adaptive mesh methods to increase the accuracy and decrease the computational time. In [3], an *h*-adaptive mesh method is contributed and demonstrate its efficiency comparing to the uniform mesh methods. Encouraged by their result and noticed that a smoothly mesh redistribution strategy

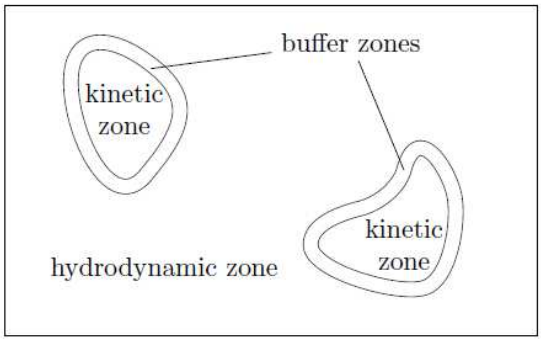

Figure 1: Domain decomposition.

takes more advantages since all the computational regions are also changing their location smoothly and continuously, we devote a moving mesh method for numerical simulations of the kinetic/hydrodynamic coupling model in this paper. Furthermore, due to the simple data structure of our mesh moving algorithm, the implementation is suitable to deal with the problems containing shock waves and boundary layers. Relevant works for the moving mesh method can be found in [7, 8, 10, 11, 30] and books [12, 13].

In this paper, we employ the moving mesh strategy proposed in [14] by using harmonic maps. The basic idea of the strategy is solving both the mesh equations and physical equations directly in the physical domain and update the physical solution after the mesh redistribution through a nonlinear interpolation. The method has been applied in many fields by finite element method, e.g., [15–18] and has been generalized to discontinuous Galerkin method in [19]. Here in order to keep the conservation of the numerical solutions of the kinetic/hydrodynamic coupling model, we adopt a finite volume scheme instead of finite element part in the moving mesh procedure. We also point out that there are other efficient methods for resolving the interface problems, e.g., interface-fitted finite element level set method [20] and anisotropic mesh refinement algorithm [21].

The outline of this paper is as follows. In Section 2, we introduce the Boltzmann-BGK equation, the coupling method and numerical schemes on a static mesh for the hybrid model. In Section 3, we briefly outline the moving mesh method with a suitable monitor function together with the hybrid model. A complete algorithm for our method is also presented in this section. Two numerical examples which demonstrate the numerical efficiency and validation of the coupling model on moving mesh are presented in Section 4. Some concluding remarks will be given in the last section.

2 The hybrid model and numerical method

2.1 The hybrid model

Let f represent the distribution of particles which have position $\boldsymbol{x} \in \Omega \subset \mathbb{R}^D$ and velocity $\boldsymbol{v} \in \mathbb{R}^D$ at time $t > 0$, where D is the dimension. Then the Boltzmann-BGK equation (cf. [22]) is

$$\begin{cases} \partial_t f + \boldsymbol{v} \cdot \nabla_{\boldsymbol{x}} f = \nu(M_f - f), \\ f(\boldsymbol{x}, \boldsymbol{v}, 0) = f_0(\boldsymbol{x}, \boldsymbol{v}), \end{cases} \tag{2.1}$$

where ν is the collision frequency. Here M_f is the Maxwellian distribution which gives the distribution of velocity of particles in local thermal equilibrium. It is defined by

$$M_f = M_f[n, \boldsymbol{u}, T](\boldsymbol{v}) = \frac{n}{(2\pi\theta)^{D/2}} \exp\Big(\frac{-|\boldsymbol{u} - \boldsymbol{v}|^2}{2\theta}\Big), \tag{2.2}$$

where n, $\boldsymbol{u}$ and T are the density, mean velocity and macroscopic temperature respectively and $\theta = RT$ with R the gas constant. These macroscopic values are related to f

by its first three moments

$$n=\int_{\mathbb{R}^D} f\mathrm{d}\boldsymbol{v},\quad n\boldsymbol{u}=\int_{\mathbb{R}^D}\boldsymbol{v}f\mathrm{d}\boldsymbol{v},\quad E=\int_{\mathbb{R}^D}\frac{1}{2}|\boldsymbol{v}|^2 f\mathrm{d}\boldsymbol{v}=\frac{1}{2}n|\boldsymbol{u}|^2+\frac{D}{2}n\theta. \tag{2.3}$$

The collision frequency ν is calculated as [3,22,23] by

$$\nu=\frac{8nT^{1-\chi}}{5\sqrt{\pi}Kn}, \tag{2.4}$$

where χ is a constant for a given gas, $Kn=\lambda_\infty/L$ is the Knudsen number with λ_∞ the mean free path of free stream and L some characteristic length.

For the kinetic/hydrodynamic coupling model, a continuous cut-off function has been introduced in [1,2] for 1-dimensional case and in [3] for 2-dimensional case. Here we will redescribe the method of [3] briefly for the completeness of the paper. One for more details is referred to [3].

Let $\Omega_1,\Omega_2,\cdots,\Omega_m$ denote the kinetic regions and B_i denotes the buffer zone with fixed width d around Ω_i, $i=1,2,\cdots,m$. A cut-off function $h(\boldsymbol{x},t)$ is then defined as follows

$$h(\boldsymbol{x},t)=\begin{cases}1, & \text{for } \boldsymbol{x}\in\Omega_i,\\ 1-\dfrac{1}{d}\min\limits_{i=1,2,\cdots,m}\mathrm{dist}(\boldsymbol{x},\Omega_i), & \text{for } \boldsymbol{x}\in B_i,\\ 0, & \text{other.}\end{cases} \tag{2.5}$$

It is commented that each Ω_i as well as the number of kinetic regions m might change as time evolution. Multiplying (2.1) by h and $1-h$ respectively leads to

$$\partial_t f_R+h\boldsymbol{v}\cdot\nabla_{\boldsymbol{x}}f=h\nu(M_f-f)+f\partial_t h, \tag{2.6a}$$

$$\partial_t f_L+(1-h)\boldsymbol{v}\cdot\nabla_{\boldsymbol{x}}f=(1-h)\nu(M_f-f)-f\partial_t h, \tag{2.6b}$$

with initial conditions

$$f_R(\boldsymbol{x},\boldsymbol{v},0)=h(\boldsymbol{x},0)f(\boldsymbol{x},\boldsymbol{v},0),\qquad f_L(\boldsymbol{x},\boldsymbol{v},0)=(1-h(\boldsymbol{x},0))f(\boldsymbol{x},\boldsymbol{v},0),$$

where $f_R=hf$ and $f_L=(1-h)f$. Multiplying (2.6b) by the vector of the collision invariants $\boldsymbol{m}=(1,\boldsymbol{v},|\boldsymbol{v}|^2/2)^T$ and integrate both sides with respect to $\boldsymbol{v}$ over $\mathbb{R}^D$, we have the following Euler equations

$$\partial_t\boldsymbol{\rho}_L+(1-h)\nabla_{\boldsymbol{x}}\cdot\int_{\mathbb{R}^D}\boldsymbol{v}\otimes\boldsymbol{m}f\mathrm{d}\boldsymbol{v}=-\boldsymbol{\rho}\partial_t h, \tag{2.7}$$

where $\boldsymbol{\rho}=(n,n\boldsymbol{u},E)^T$ is the first three moments of f and $\boldsymbol{\rho}_L=(1-h)\boldsymbol{\rho}$. Then the hybrid model is completed by (2.6a) and (2.7) with initial conditions

$$f_R(\boldsymbol{x},\boldsymbol{v},0)=h(\boldsymbol{x},0)f(\boldsymbol{x},\boldsymbol{v},0),\qquad \boldsymbol{\rho}_L(\boldsymbol{x},0)=\int_{\mathbb{R}^D}\boldsymbol{m}(\boldsymbol{v})f_L(\boldsymbol{x},\boldsymbol{v},0)\mathrm{d}\boldsymbol{v}.$$

2.2 Numerical methods on a static mesh

The hybrid model is first discretized in velocity space using the discrete velocity model [24] and the resulting equations are then solved with finite volume schemes in spatial domain. In the following of the paper, we introduce our method in two dimensional case to simplify our discussion.

Suppose $\Sigma \in \mathbb{R}^2$ to be a disc for velocity $\boldsymbol{v}$ with its center at origin and radius $v_{\max}$, i.e.,

$$\Sigma = \big\{(r,\varphi)|0 \le r \le v_{\max},\ \ 0 \le \varphi < 2\pi\big\}$$

under polar coordinates (r,φ). The mesh to discrete velocity $\boldsymbol{v}$ on Σ is a uniform one that all the mesh points form a set

$$\mathcal{V} = \big\{(i\Delta r, j\Delta\varphi)|i = 1,\cdots,M;\ \ j = 1,\cdots,N\big\} \cup \big\{(0,0)\big\}$$

with $M\Delta r = v_{\max}$, $N\Delta\varphi = 2\pi$. Denoting each mesh point on Σ by $\boldsymbol{v}_k$ and K the total number of mesh points, i.e., $K = MN + 1$, we take the same numerical quadrature formula as [3] over velocity space Σ by

$$\int_\Sigma f(\boldsymbol{v})\mathrm{d}\boldsymbol{v} = \sum_{k=1}^{K} \omega_k f(\boldsymbol{v}_k), \tag{2.8}$$

where the weights ω_k are chosen in order to be accurate for piecewise biquadratic function. The following nine points formula

$$\int_{r^0}^{r^1} \mathrm{d}r \int_{\varphi^0}^{\varphi^1} rf(r,\varphi)\mathrm{d}\varphi = \frac{(r^1-r^0)(\varphi^1-\varphi^0)}{36} \sum_{i=0}^{2}\sum_{j=0}^{2} c_i c_j r^{\frac{i}{2}} f(r^{\frac{i}{2}}, \varphi^{\frac{j}{2}}) \tag{2.9}$$

is accurate for biquadratic function over a rectangle $[r^0,r^1]\times[\varphi^0,\varphi^1]$. Here $c_0 = c_2 = 1$, $c_1 = 4$ and $r^{1/2} = (r^0+r^1)/2$, $\varphi^{1/2} = (\varphi^0+\varphi^1)/2$. Let both M and N be even, then the weights ω_k can be calculated through (2.9) and the following formula

$$\int_\Sigma f(\boldsymbol{v})\mathrm{d}\boldsymbol{v} = \int_\Sigma rf(r,\varphi)\mathrm{d}r\mathrm{d}\varphi = \sum_{i=1}^{M/2}\sum_{j=1}^{N/2} \int_{2(i-1)\Delta r}^{2i\Delta r} \mathrm{d}r \int_{2(j-1)\Delta\varphi}^{2j\Delta\varphi} rf(r,\varphi)\mathrm{d}\varphi. \tag{2.10}$$

From the H-Theorem (cf. [25]) it is well known that the Maxwellian distribution M_f minimizes the entropy functional

$$\mathcal{H}(f) = \int_{\mathbb{R}^2} f\log f\mathrm{d}\boldsymbol{v}, \tag{2.11}$$

where f satisfies (2.3). As in [24], the discrete Maxwellian, denoting by $\mathcal{E}_k$ at $\boldsymbol{v}_k$, can be defined to minimize the discrete entropy functional of (2.11)

$$\mathcal{E}_{\mathcal{K}} = \arg\min_{g\in\mathbb{R}^K}\Big\{\sum_{k=1}^{K}\omega_k g_k\log g_k : g \ge 0, \quad \boldsymbol{\rho} = \sum_{k=1}^{K}\boldsymbol{m}_k g_k\omega_k\Big\}, \tag{2.12}$$

where $\boldsymbol{m}_k = (1, \boldsymbol{v}_k, |\boldsymbol{v}_k|^2/2)^T$ and ω_k is the weight of the quadrature formula (2.8). The unique solution of (2.12) has the following form [24]

$$\mathcal{E}_k = \exp(\boldsymbol{\alpha} \cdot \boldsymbol{m}_k), \quad k = 1, 2, \cdots, K, \tag{2.13}$$

where $\boldsymbol{\alpha} \in \mathbb{R}^4$ satisfying

$$\sum_{k=1}^{K} \boldsymbol{m}_k \exp(\boldsymbol{\alpha} \cdot \boldsymbol{m}_k)\omega_k = \boldsymbol{\rho}. \tag{2.14}$$

With initial guess as

$$\boldsymbol{\alpha}^{(0)} = \Big(\log\Big(\frac{n}{(2\pi\theta)^{D/2}}\Big) - \frac{|\boldsymbol{u}|^2}{2\theta}, \frac{\boldsymbol{u}}{\theta}, -\frac{1}{\theta} \Big)^T, \tag{2.15}$$

the solution of (2.14) can be obtained in only a few steps of Newton iteration.

After discretized in velocity space, we employ the standard upwind finite volume scheme for spatial space and the explicit Euler method for time integration, to make our numerical simulations easier to be implemented. Additionally, the spatial discretization is applied on an unstructured triangular mesh for it is more applicable to domains with complex shapes and the time step Δt is computed to satisfy the CFL condition by

$$\Delta t \Big(\max_i(\nu_i) + \max_k \Big(\frac{|\boldsymbol{v}_k|}{l}\Big) \Big) < 1, \tag{2.16}$$

where l is the minimum length in all edges of the triangulation. As pointed out in [3], a time unsplit method is more difficult to make it work on the adaptive meshes. Hence we use the time-split scheme for our implementation. Finally, the scheme reads

$$f_{k,i,R}^{n+\frac{1}{2}} = h_i^{n+1} f_{k,i}^n, \tag{2.17a}$$

$$f_{k,i,R}^{n+1} = f_{k,i,R}^{n+\frac{1}{2}} - \Delta t \Big[\frac{1}{|\Delta_i|} \sum_j h_{ij}^{n+1} l_{ij} \phi_{i,j}(f_{k,i_j}^n, f_{k,i}^n) - h_i^{n+1} \nu_i^n (\mathcal{E}_k[\boldsymbol{\rho}^n] - f_{k,i}^n) \Big], \tag{2.17b}$$

for the kinetic part and similarly

$$\boldsymbol{\rho}_{i,L}^{n+\frac{1}{2}} = (1 - h_i^{n+1}) \boldsymbol{\rho}_i^n, \tag{2.18a}$$

$$\boldsymbol{\rho}_{i,L}^{n+1} = \boldsymbol{\rho}_{i,L}^{n+\frac{1}{2}} - \frac{\Delta t}{|\Delta_i|} \sum_{k=1}^{K} \boldsymbol{m}_k \omega_k \sum_j (1 - h_{ij}^{n+1}) l_{ij} \phi_{i,j}(f_{k,i_j}^n, f_{k,i}^n), \tag{2.18b}$$

for the hydrodynamic part. Here $|\Delta_i|$ is the area of the ith element, l_{ij} is the length of the jth boundary of element i and i_j is the index of the jth neighbour of element i. The cut-off function h^{n+1} for the $n+1$ time step will be constructed before applying the scheme and h_i, h_{ij} are the mean values of the cut-off function on the ith element and on its jth boundary, respectively. The numerical flux of upwind scheme is given by

$$\phi_{i,j}(f_k^L, f_k^R) = \frac{1}{2}\big[(\boldsymbol{v}_k \cdot \boldsymbol{n}_{i,j})(f_k^L + f_k^R) - |\boldsymbol{v}_k \cdot \boldsymbol{n}_{i,j}|(f_k^L - f_k^R)\big], \tag{2.19}$$

where $\boldsymbol{n}_{i,j}$ is the unit out normal on the jth boundary of ith element.

However, the computational cost of the hydrodynamic part of the scheme (2.18a) and (2.18b) is no less than the scheme in kinetic zones. In the pure hydrodynamic regions, where the fluids are close to the thermodynamical equilibrium, it is possible to use a more efficient method, while maintaining the same accuracy. We use the Perthame scheme [26] in the pure hydrodynamic regions to obtain considerable acceleration. Followed by [3], the Maxwellian M_f is substituted by a simpler function given by

$$M(\boldsymbol{v}) = \begin{cases} \tilde{\alpha}, & |\boldsymbol{v}-\boldsymbol{u}| \le \tilde{\beta}, \\ 0, & \text{others}, \end{cases} \tag{2.20}$$

where $\tilde{\alpha} = n/4\pi\theta$, $\tilde{\beta} = \sqrt{4\theta}$ such that the Eqs. (2.3) still hold for $f = M(\boldsymbol{v})$. Then in the pure hydrodynamic regions where $h = 0$, the scheme reads

$$\begin{aligned} \boldsymbol{\rho}_i^{n+1} &= \boldsymbol{\rho}_i^n - \frac{\Delta t}{|\Delta_i|}\sum_j l_{ij}\int_{\mathbb{R}^2} \boldsymbol{m}\phi_{i,j}(M_{i_j}^n, M_i^n)\mathrm{d}\boldsymbol{v} \\ &= \boldsymbol{\rho}_i^n - \frac{\Delta t}{|\Delta_i|}\sum_j l_{ij}\Big[\int_{\mathbb{R}_{i,j}^{2+}} \boldsymbol{m}(\boldsymbol{v}\cdot\boldsymbol{n}_{i,j})M_i^n\mathrm{d}\boldsymbol{v} + \int_{\mathbb{R}_{i,j}^{2-}} \boldsymbol{m}(\boldsymbol{v}\cdot\boldsymbol{n}_{i,j})M_{i_j}^n\mathrm{d}\boldsymbol{v}\Big], \end{aligned} \tag{2.21}$$

where $\mathbb{R}_{i,j}^{2\pm} = \{\boldsymbol{v}|\boldsymbol{v}\cdot\boldsymbol{n}_{i,j} \gtrless 0\}$. The integral in (2.21) can be calculated analytically [3] thus more faster than the scheme (2.18a) and (2.18b).

If the hydrodynamic part of the scheme (2.18a) and (2.18b) is used in the buffer zones, numerical oscillations will be observed on the interface between pure hydrodynamic regions and buffer zones due to incompatible of the two hydrodynamic schemes. To obtain a compatible scheme of the hydrodynamic part in the buffer zones to the scheme (2.21) in the pure hydrodynamic regions, both hydrodynamic schemes are applied in the buffer zones, which is reused as a transitional buffer between two hydrodynamic schemes. The final hydrodynamic scheme in the buffer zones reads

$$\begin{aligned} \boldsymbol{\rho}_{i,L}^{n+1} = KS(\boldsymbol{\rho}_{i,L}^n, h^{n+1}f^n) - \frac{\Delta t}{|\Delta_i|}\sum_j (1-h_{ij}^{n+1})^2 l_{ij}\Big[\int_{\mathbb{R}_{i,j}^{2+}} \boldsymbol{m}(\boldsymbol{v}\cdot\boldsymbol{n}_{i,j})M_i^n\mathrm{d}\boldsymbol{v} \\ + \int_{\mathbb{R}_{i,j}^{2-}} \boldsymbol{m}(\boldsymbol{v}\cdot\boldsymbol{n}_{i,j})M_{i_j}^n\mathrm{d}\boldsymbol{v}\Big], \end{aligned} \tag{2.22}$$

where KS is the kinetic Euler solver (2.18a) and (2.18b) with f^n in it replaced by $h^{n+1}f^n$. Now the whole scheme becomes compatible and conservative.

We conclude this section by identifying the kinetic zones and constructing h at every time step. In the kinetic zones at current time step. If the L^1 norm of the difference between the discrete distribution and discrete Maxwellian

$$\beta_{M,i} = 1 - \frac{1}{n}\sum_{k=1}^{K} |f_{k,i} - \mathcal{E}_k[\boldsymbol{\rho}_i]|\omega_k \tag{2.23}$$

is not close enough to 1, which means the fluids are far away from the thermodynamical equilibrium, the ith element is identified as kinetic at the next time step. And in the

regions out of the kinetic zones, the hydrodynamic breakdown parameter proposed in [27] takes the form

$$Kn_{\max} = \max\left\{Kn_n, Kn_T, Kn_V\right\}, \tag{2.24}$$

where

$$Kn_Q = \lambda \frac{|\nabla Q|}{Q}, \quad Q \in \{n, T, V\}, \tag{2.25}$$

with the mean free path λ and the magnitude of velocity V. If $Kn_{\max}$ is bigger than a problem dependent threshold, the corresponding element is marked as kinetic region at the next time step. While all kinetic zones have been identified, the cut-off function h can be constructed without any difficulty. In our implementation, h is approximated by a piecewise linear and continuous function on the spatial mesh which can be obtained very cheaply.

3 Coupled with moving mesh method

In this section, we couple the hybrid model in previous section with moving mesh method to obtain a more efficient solver. We follow the moving mesh framework introduced by [14, 28], in which moving mesh method is divided into two independent parts, namely mesh redistribution and PDE evolution. we briefly outline the moving mesh procedure and concentrate on several key ingredients, which will be encountered during our implementation for the hybrid model. we will conclude this section with a complete algorithm of the numerical method for the final coupling system.

3.1 Moving mesh strategy

Denote Ω as the physical domain and Ω_c as the logical domain. A one-to-one mapping $\boldsymbol{\xi} = \boldsymbol{\xi}(\boldsymbol{x})$ from Ω to Ω_c can be achieved by solving the Euler-Lagrange system

$$\frac{\partial}{\partial x_i}\left(G^{ij}\frac{\partial \boldsymbol{\xi}}{\partial x_j}\right) = 0, \quad \boldsymbol{x} \in \Omega, \tag{3.1a}$$

$$\boldsymbol{\xi}|_{\partial\Omega} = \boldsymbol{\xi}_b \in \mathrm{K}, \tag{3.1b}$$

where $M = G^{-1} = (G^{ij})^{-1}$ is the so-called monitor function and K is the admissible set for the boundary mappings. If we choose Ω_c such that its Riemannian curvature is nonpositive and its boundary is convex, then existence and uniqueness of $\boldsymbol{\xi}(\boldsymbol{x})$ are guaranteed. The inverse of $\boldsymbol{\xi}(\boldsymbol{x})$ determines a mesh on Ω from a regular mesh on Ω_c.

Assume we have obtain the mesh $\boldsymbol{x}^{(n)}$ and the numerical solutions of PDEs under consideration, i.e., $\boldsymbol{\rho}^{(n)}$, $f^{(n)}$, at $t = t^n$. The diagram of the moving mesh procedure to obtain the new mesh $\boldsymbol{x}^{(n+1)}$ and solutions on it is given in Fig. 2. Here, $\boldsymbol{\xi}^{(0)}$ is the fixed initial mesh on Ω_c, generated by solving the Poisson equation $\Delta\boldsymbol{\xi} = 0$ with some Dirichlet boundary condition and $\eta \in [0, 1]$ is a suitable ratio parameter to prevent mesh tangling. The strategy is an iterative procedure which will be finished up until

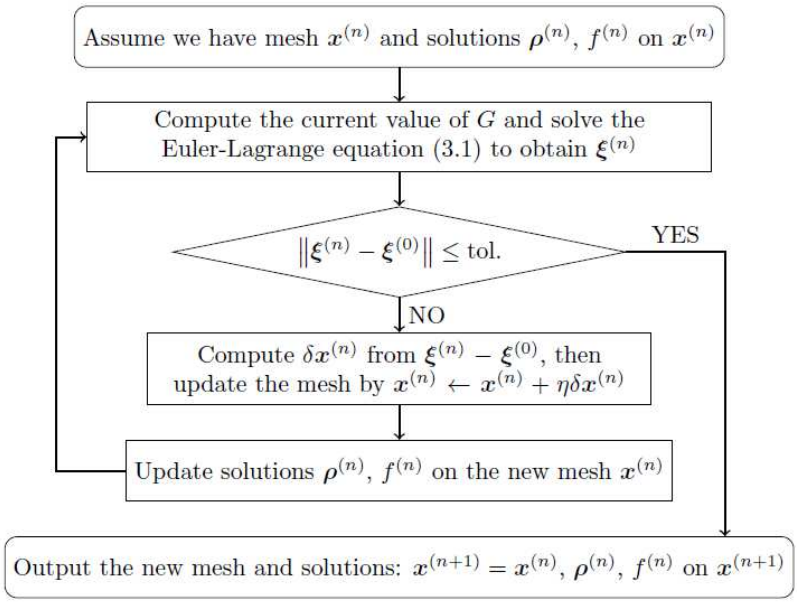

Figure 2: Moving mesh procedure.

$\|\xi^{(n)} - \xi^{(0)}\|$ is small enough. In general, this iterative procedure will be end up in very small steps with a proper selected monitor function.

3.2 Monitor function

The monitor function plays an important role in moving mesh method and should be selected carefully [29].

It is problem dependent and is usually chosen to involve solution information for special consideration or an posteriori error.

The most advocated monitor function is first proposed by Winslow [32] with the form of a scalar matrix function

$$M = mI,$$

where $m = m(x)$ is a positive scalar function. The mesh generated from this monitor function is isotropic since the eigenvalues of M are all equal. Due to our solutions of the problem are piecewise constant functions on the mesh, the most general choice of the arclength like monitor could not work here. Analogue to the choice in [19] for moving mesh discontinuous Galerkin method, the following monitor is chosen in our implementation

$$m_i = \sqrt{\tilde{\eta} + \alpha\eta_i}, \tag{3.2}$$

where

$$\eta_i = \frac{1}{|\Delta_i|} \sum_{e \in \partial\Delta_i} \int_e |p_i - p_{i,e}| \mathrm{d}s \tag{3.3}$$

is a reasonable indicator for the error of the numerical approximation on the ith element and

$$\tilde{\eta} = \frac{1}{|\Omega|}\int_{\Omega}\eta \mathrm{d}\boldsymbol{x} \tag{3.4}$$

is the average of the indicator function η. Here p_i, $p_{i,e}$ are the pressure on the ith element and its neighbour with boundary e. The parameter $\alpha > 0$ is a user-define parameter to control the ratio of the maximal and minimal element sizes. Noticed that the jump of the pressure across the edge of elements is about $\mathcal{O}(h)$ if the pressure is a smooth function, the formal order of this monitor function is $\mathcal{O}(1)$, that is, our monitor is mesh independent.

In practice, local (spatial) smoothing of the monitor function is necessary to enhance the quality of the mesh (see e.g., [29–31]). According to the experience, the number of smoothing steps is set to be the largest integer not greater than $\sqrt{\#\text{ nodes}/5}$ such that the smoothing monitor is almost mesh independent [19].

3.3 Update solutions on the new mesh

After we obtain the new mesh, all numerical solutions need to be interpolated onto the new mesh from the old one. Let u denote the solution of the general PDE and $\overrightarrow{\delta x}$ is the vector representing the node-displacement between the new mesh and the old mesh. We introduce a parameter $\tau \in [0,1]$ such that the old mesh is transited into the new mesh continuously with the velocity $\overrightarrow{\delta x}$ as τ from 0 to 1. That is, we introduce a linear transformation $X(\tau) = X_{\text{old}} + \tau\overrightarrow{\delta x}$ with $X(0)$ the old mesh and $X(1)$ the new mesh. Then the solution on the new mesh can be obtained by solving the following linear convection PDE

$$\frac{\partial u}{\partial \tau} - \overrightarrow{\delta x}\cdot\nabla u = 0. \tag{3.5}$$

With this PDE-based interpolation, the solution will preserve its L^2 norm [33].

Similar to [19], the above equation will be solved by using the finite volume scheme so that the solution conservation is preserved. The form of the upwind finite volume scheme to (3.5) takes

$$\begin{aligned} u_i^{n+1} &= u_i^n + \frac{\delta\tau}{|\Delta_i|}\Big[\sum_{e\in\partial\Delta_i}\int_e u^n\overrightarrow{\delta x}\cdot\boldsymbol{n}\mathrm{d}s - \int_{\Delta_i}u^n\nabla\cdot\overrightarrow{\delta x}\mathrm{d}\boldsymbol{x}\Big] \\ &= u_i^n + \frac{\delta\tau}{|\Delta_i|}\sum_j l_{ij}F_{i,j}(u_i^n, u_{i_j}^n) - \delta\tau u_i^n\nabla\cdot\overrightarrow{\delta x}, \end{aligned} \tag{3.6}$$

where the flux is

$$F_{i,j}(u_i, u_{i_j}) = \frac{1}{2}\big[(\overrightarrow{\delta x}\cdot\boldsymbol{n}_{i,j})(u_i + u_{i_j}) - |\overrightarrow{\delta x}\cdot\boldsymbol{n}_{i,j}|(u_i - u_{i_j})\big]. \tag{3.7}$$

Both the hydrodynamic and microscopic quantities are updated by this upwind scheme.

Since the microscopic quantities are only well defined in the kinetic zones and buffer zones, it is inefficient to update them in the whole domain. And another problem is for the mesh grids moving from the hydrodynamic zone into the buffer zone, we still do not have the microscopic quantities to update. To solve those problems, we update the cut-off function h to the new mesh first, then we can only update the microscopic quantities on the kinetic and buffer zones which are identified by the cut-off function.

As h is an artificial function to identify the domain decomposition, it does not require an accurate and complicated calculation. Instead, we compute the value of h on node X_j of the new mesh by the following formula

$$h_j = \frac{\int_\Omega h_{\text{old}} \phi_j \mathrm{d}\boldsymbol{x}}{\int_\Omega \phi_j \mathrm{d}\boldsymbol{x}}, \tag{3.8}$$

where h_{old} represents the cut-off function on the old mesh and ϕ_j is the piecewise linear basis function satisfying $\phi_j(X_i) = \delta_{ij}$ with X_i the node of the new mesh. With formula (3.8), the cut-off function on the new mesh can be obtained cheaply while keep its L^1 norm. And this has been implemented in the open source package AFEPack [34].

For the mesh grids moving into buffer zones from hydrodynamic zones, the microscopic quantities is unknown at $\tau = 0$. As these grids are located in hydrodynamic zones before mesh movement, where the distribution f is close to the local Maxwellian, we can employ its Maxwellian as the initial values of the microscopic quantities at $\tau = 0$.

We conclude this section with a full algorithm for the hybrid model coupled with the moving mesh method. The diagram of the algorithm is shown in Fig. 3.

4 Numerical examples

In this section, we present two numerical examples to illustrate the efficiency of our method using the open source package AFEPack [34]. The initial uniform meshes on the space domain are generated by the software Easymesh [35]. For simplicity, Maxwell gas is considered, i.e., $\chi = 1$ in (2.4) and the gas obey the gamma law with $\gamma = 2$ in these examples so that the Maxwellian distribution satisfies (2.2).

The parameter to compute the monitor function (3.2) is $\alpha = 2$ for the first example and $\alpha = 5$ for the second. In practice, the moving mesh works well when the logical domain is identical with the physical domain, although there is no theoretical guarantee. And in the following examples, we take the physical domain and the logical domain be the same.

4.1 Shock diffraction around a cylinder

This problem was studied by Yang and Huang [22] and has been used as a benchmark problem. It has been investigated for the hybrid model on the fixed mesh in [1] and on

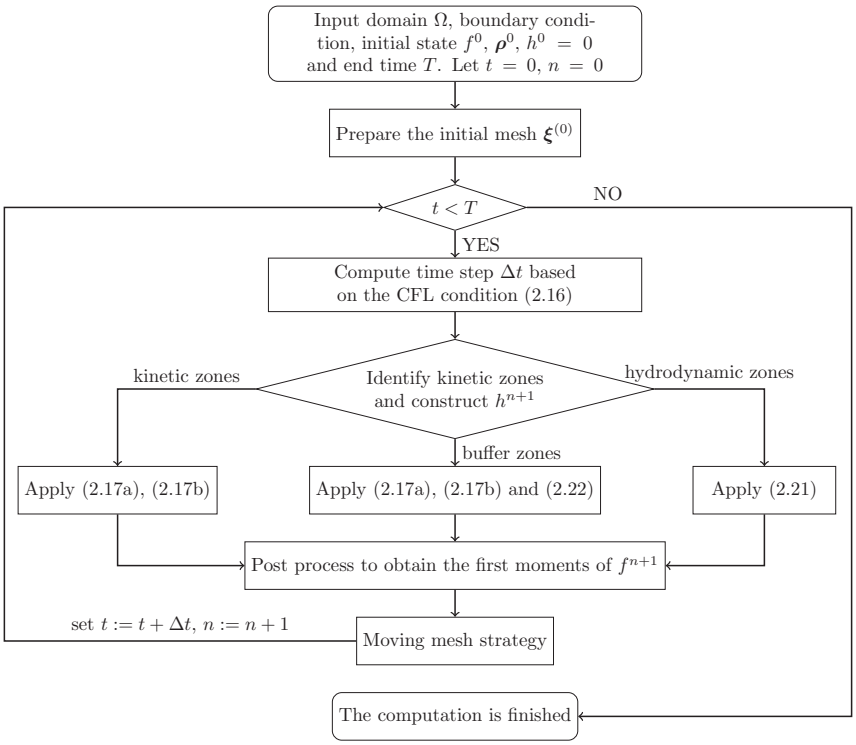

Figure 3: The hybrid model solver coupled with the moving mesh method.

the h-adaptive mesh in [3]. The data of this example are taken from [3]. The computational domain is set to be $[-3,5] \times [-5,5]$. The circular cylinder is centered at $(0.5,0)$, with radius be 0.5. The shock is located at $x = -1$ in initial time and transferred to right with the Mach number be 2.81. The initial conditions of the undisturbed right state are

$$n = 1, \qquad \boldsymbol{u} = (0,0)^T, \qquad \theta = 1,$$

and the left state ahead of the shock are computed by the Rankine-Hugoniot condition. The Knudsen number is $Kn = 0.005$.

Ghost cells are employed for the boundary conditions. On the edge of the outer rectangle, the states in ghost cells and the area of the ghost cells are set to be identical with the corresponding boundary cells. The pure specularly reflective boundary conditions are used on the wall of the cylinder. The velocity mesh is on the disc with the radius $v_{\max} = 8$ and $M = N = 40$. Due to the symmetry, only the half plane is computed and symmetry boundary conditions are enforced on the artificial boundary.

Fig. 4 shows the initial uniform mesh for the example, which has 6044 grids.

It is compared with [3] and much less than that in [1,22]. However, the numerical results are compared to the figures in [3] and more closer to that in [22] than in [1]. This indicates the efficiency of our method.

The evolution of the density contours, meshes and corresponding kinetic zones at

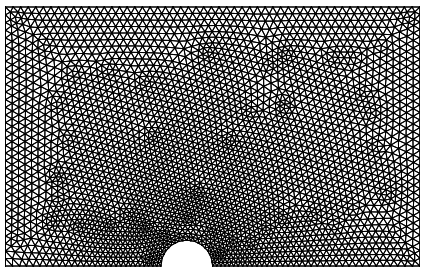

Figure 4: The initial uniform mesh.

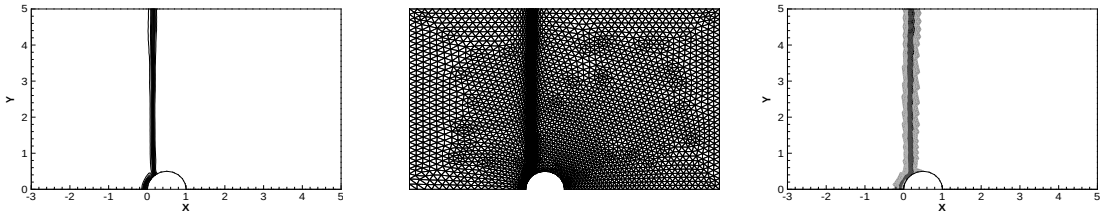

(a) Density contours (b) Mesh on the physical domain (c) Domain decomposition

Figure 5: The density, mesh and decomposition of the physical domain at $t = 0.4$.

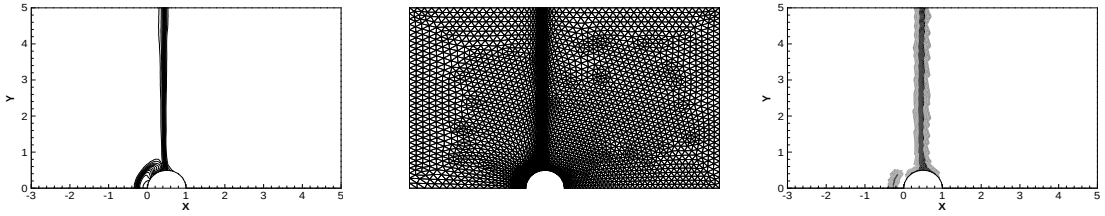

(a) Density contours (b) Mesh on the physical domain (c) Domain decomposition

Figure 6: The density, mesh and decomposition of the physical domain at $t = 0.5$.

different times are shown in Figs. 5-11, where the kinetic, buffer and hydrodynamic zones are black, gray and white, respectively. We can see that the primary incident shock, the reflected bow shock and the Mach shock can all be identified. The results are similar with that based on *h*-adaptive method and the full kinetic results given in [3]. The reflected bow shock is also not identified as kinetic, since both high density and temperature on the shock leads its distribution much closer to the Maxwellian than the other two shocks.

4.2 Mach 3 flow past a forward facing step

In this section, we consider flow in a wind tunnel containing a step which begin with uniform Mach 3 flow. The wind tunnel is set to have width 1 and length 3. The step is located 0.6 from the left end of the tunnel with height 0.2. The tunnel is filled with

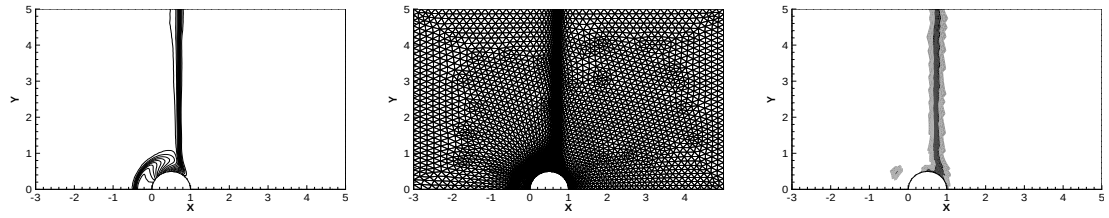

(a) Density contours (b) Mesh on the physical domain (c) Domain decomposition

Figure 7: The density, mesh and decomposition of the physical domain at $t = 0.6$.

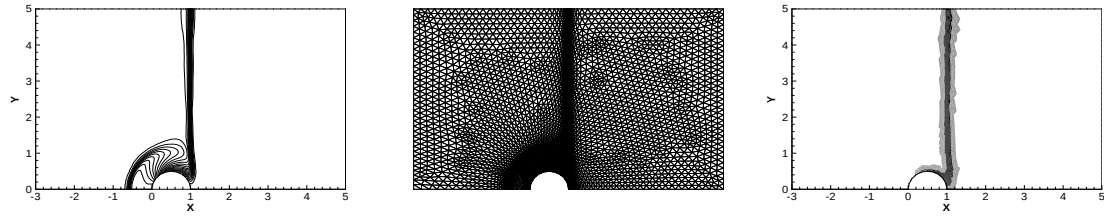

(a) Density contours (b) Mesh on the physical domain (c) Domain decomposition

Figure 8: The density, mesh and decomposition of the physical domain at $t = 0.7$.

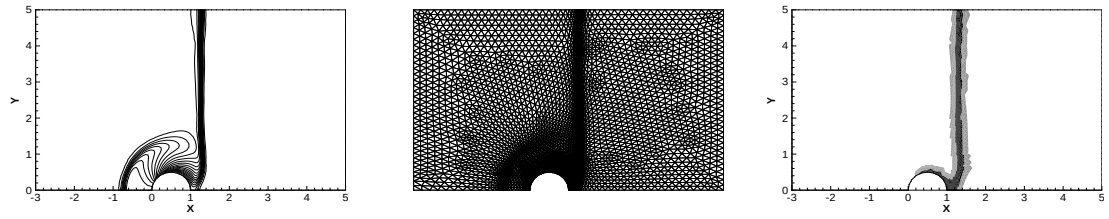

(a) Density contours (b) Mesh on the physical domain (c) Domain decomposition

Figure 9: The density, mesh and decomposition of the physical domain at $t = 0.8$.

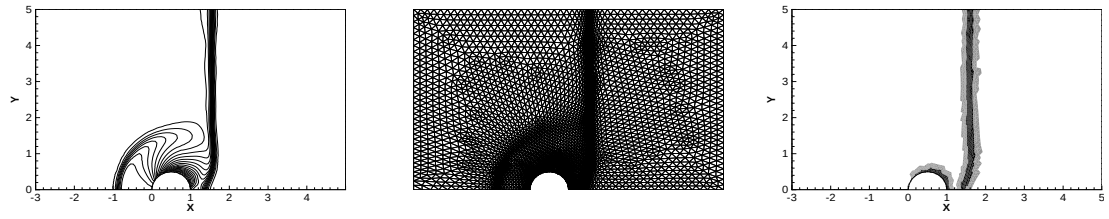

(a) Density contours (b) Mesh on the physical domain (c) Domain decomposition

Figure 10: The density, mesh and decomposition of the physical domain at $t = 0.9$.

an equilibrium gas, i.e., $(n, u_1, u_2, p) = (1.4, 3.0, 0.0, 1.0)$, at the beginning time. On the left and right boundary, the states are set to satisfy the inflow and outflow conditions,

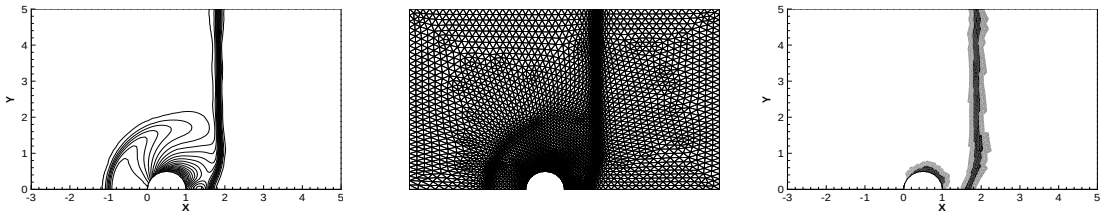

(a) Density contours (b) Mesh on the physical domain (c) Domain decomposition

Figure 11: The density, mesh and decomposition of the physical domain at $t = 1.0$.

respectively. Along the walls of the tunnel, specularly reflective boundary conditions are used. Nothing special is treated at the step corner. Additionally, the Knudsen number is $Kn = 0.01$ and the gamma law is $\gamma = 2$.

This problem was studied by Woodward and Colella [36] and has become a commonly used test problem for fluid algorithms since then. The conditions stated above agree with [36] except that we set $\gamma = 2.0$ instead of $\gamma = 1.4$. This makes our results can not compare with which presented in [36]. Hence, we compare our results with that in [3], which use the package AMROC's results [37] to validate their algorithm.

We prepare our initial adaptive mesh based on the solution after one small time step. The resulting mesh is presented in Fig. 12 with the logical mesh given in Fig. 13. In practice, it is better than the solution begin with the uniform mesh, because the solution dramatically change at the beginning time from the uniform state. The mesh preserves 8517 grids during time evolutions. Figs. 14-16 present the evolution of the density contours, meshes and corresponding kinetic zones at different times, i.e., $t = 0.4, 0.8, 1.2$, where the kinetic, buffer and hydrodynamic zones are black, gray and white, respectively.

These show that the structures of the shock agree with [3] perfectly. The first reflecting shock and the part above the step and near the corner are always identified as kinetic.

5 Conclusions

In this paper, we develop a moving mesh method for kinetic/hydrodynamics coupling model in two dimensions. In the hybrid model, the domain is decomposed into three parts and different schemes are used in each part, then all three parts are coupled automatically with a cut-off function without any internal boundary conditions. Driven by the numerical solutions of this model, with a well defined monitor function, our mesh grids are smoothly redistributed by solving an elliptic boundary problem at each time step to concentrate the grids near to the singularity of the numerical solution, which are always corresponding to the kinetic zones. To keep the total algorithm conservative, a finite volume scheme is employed in both the time evolution step of the physical equations and solution update step of the moving mesh procedure. The

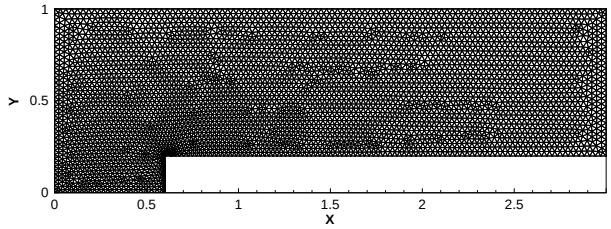

Figure 12: The initial mesh for forward facing step.

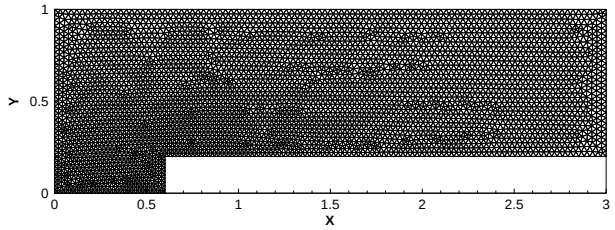

Figure 13: The logical mesh for forward facing step.

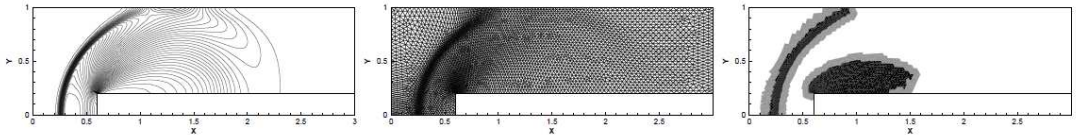

Figure 14: The density, mesh and decomposition of the physical domain at $t = 0.4$.

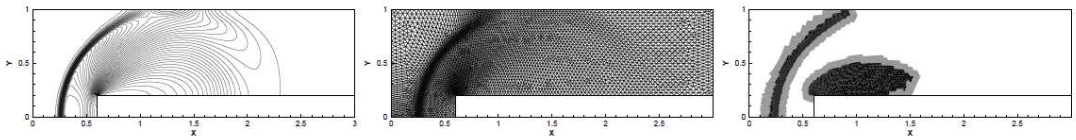

Figure 15: The density, mesh and decomposition of the physical domain at $t = 0.8$.

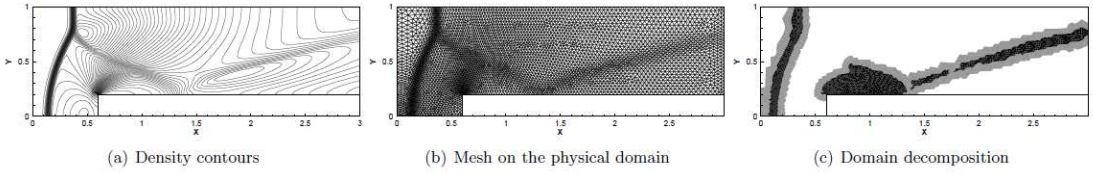

Figure 16: The density, mesh and decomposition of the physical domain at $t = 1.2$.

whole algorithm framework shows the advantages of our moving mesh strategy in deal with the complex physical models and the well performs of the numerical simulations in Section 4 demonstrated the validation and the efficiency of our method. An extension of the algorithm to three dimensions is in our future research.

Acknowledgments

This work was partially supported by a grant of key program from the National Natural Science Foundation of China (No. 10731060, 10801120), National Basic Research Program of China (2011CB309704) and Chinese Universities Scientific Fund No. 2010QNA3019.

References

[1] P. DEGOND, S. JIN AND L. MIEUSSENS, *A smooth transition model between kinetic and hydrodynamic equations*, J. Comput. Phys., 209(2) (2005), pp. 665–694.
[2] P. DEGOND, G. DIMARCO AND L. MIEUSSENS, *A moving interface method for dynamic kinetic-fluid coupling*, J. Comput. Phys., 227(2) (2007), pp. 1176–1208.
[3] Z. CAI AND R. LI, *An h-adaptive mesh method for Boltzmann-BGK/hydrodynamics coupling*, J. Comput. Phys., 229(5) (2010), pp. 1661–1680.
[4] Z. CAI, R. LI AND Y. WANG, *Numerical regularized moment method for high Mach number flow*, Commun. Comput. Phys., 11 (2012), pp. 1415–1438.
[5] A. PASSALACQUA, J. E. GALVIN, P. VEDULA, C. M. HRENYA AND R. O. FOX, *A quadrature-based kinetic model for dilute non-isothermal granular flows*, Commun. Comput. Phys., 10 (2011), pp. 216–252.
[6] M. GREGORY FOREST, Q. LIAO AND Q. WANG, *A 2-D kinetic theory for flows of monodomain polymer-rod nanocomposites*, Commun. Comput. Phys., 7 (2010), pp. 250–282.
[7] M. J. BAINES, M. E. HUBBARD AND P. K. JIMACKI, *Velocity-based moving mesh methods for nonlinear partial differential equations*, Commun. Comput. Phys., 10 (2011), pp. 509–576.
[8] C.-Q. JIN, K. XU AND S. CHEN, *A three dimensional gas-kinetic scheme with moving mesh for low-speed viscous flow computations*, Adv. Appl. Math. Mech., 2 (2010), pp. 746–762.
[9] K. XU, J. LUO AND S. CHEN *A well-balanced kinetic scheme for gas dynamic equations under gravitational field*, Adv. Appl. Math. Mech., 2 (2010), pp. 200–210.
[10] Y.-B. ZHANG, H.-Y. WANG AND T. TANG, *Simulating two-phase viscoelastic flows using moving finite element methods*, Commun. Comput. Phys., 7 (2010), pp. 333–349.
[11] Y.-B. ZHANG AND T. TANG, *Simulating three-dimensional free surface viscoelastic flows using moving finite difference schemes*, Numer. Math. Theor. Meth. Appl. 4 (2011), pp. 92–112.
[12] T. TANG AND J. XU, Adaptive Computations: Theory and Algorithms, Science Press, 2007.
[13] W. Z. HUANG AND R. D. RUSSELL, Adaptive Moving Mesh Methods, Springer Science+Business Media, LLC, 2011.
[14] R. LI, T. TANG AND P. ZHANG, *Moving mesh methods in multiple dimensions based on harmonic maps*, J. Comput. Phys., 170(2) (2001), pp. 562–588.
[15] H. WANG, R. LI AND T. TANG, *Efficient computation of dendritic growth with r-adaptive finite element methods*, J. Comput. Phys., 227(12) (2008), pp. 5984–6000.
[16] Z. H. QIAO, *Numerical investigations of the dynamical behaviors and instabilities for the Gierer-Meinhardt system*, Commun. Comput. Phys., 3 (2008), pp. 406–426.
[17] Y. DI, R. LI, T. TANG AND P. ZHANG, *Moving mesh finite element methods for the incompressible Navier-Stokes equations*, SIAM J. Sci. Comput., 26(3) (2005), pp. 1036–1056.
[18] Y. DI, R. LI AND T. TANG, *A general moving mesh framework in 3D and its application for simulating the mixture of multi-phase flows*, Commun. Comput. Phys., 3(3) (2008), pp. 582–602.

[19] R. LI AND T. TANG, *Moving mesh discontinuous Galerkin method for hyperbolic conservation laws*, J. Sci. Comput., 27(1) (2006), pp. 347–363.
[20] B. LI AND J. SHOPPLE, *An interface-fitted finite element level set method with application to solidification and solvation*, Commun. Comput. Phys., 10 (2011), pp. 32–56.
[21] D. WANG, R. LI AND N.-N. YAN, *An edge-based anisotropic mesh refinement algorithm and its application to interface problems*, Commun. Comput. Phys., 8 (2010), pp. 511–540
[22] J. Y. YANG AND J. C. HUANG, *Rarefied flow computations using nonlinear model Boltzmann equations*, J. Comput. Phys., 120(2) (1995), pp. 323–339.
[23] J. C. HUANG, K. XU AND P.-B. YU, *A unified gas-kinetic scheme for continuum and rarefied flows II: multi-dimensional cases*, Commun. Comput. Phys., 12 (2012), pp. 662–690.
[24] L. MIEUSSENS, *Discrete velocity model and implicit scheme for the BGK equation of rarefied gas dynamics*, Math. Models Methods Appl. Sci., 10(8) (2000), pp. 1121–1149.
[25] C. CERCIGNANI, R. ILLNER AND M. PULVIRENTI, The Mathematical Theory of Dilute Gases, Volume 106, Springer, 1994.
[26] B. PERTHAME, *Boltzmann type schemes for gas dynamics and the entropy property*, SIAM J. Numer. Anal., 27(6) (1990), pp. 1405–1421.
[27] W. L. WANG AND I. D. BOYD, *Predicting continuum breakdown in hypersonic viscous flows*, Phys. Fluids, 15(1) (2003), pp. 91–100.
[28] R. LI, T. TANG AND P. ZHANG, *A moving mesh finite element algorithm for singular problems in two and three space dimensions*, J. Comput. Phys., 177(2) (2002), pp. 365–393.
[29] W. CAO, W. HUANG AND R. D. RUSSELL, *A study of monitor functions for two-dimensional adaptive mesh generation*, SIAM J. Sci. Comput., 20(6) (1999), pp. 1978–1994.
[30] A. VAN DAM AND P. A. ZEGELING, *Balanced monitoring of flow phenomena in moving mesh methods*, Commun. Comput. Phys., 7 (2010), pp. 138–170.
[31] P. A. ZEGELING, I. LAGZI AND F. IZSK, *Transition of Liesegang precipitation systems: simulations with an adaptive grid PDE method*, Commun. Comput. Phys., 10 (2011), pp. 867–881.
[32] A. M. WINSLOW, *Numerical solution of the quasilinear Poisson equation in a nonuniform triangle mesh*, J. Comput. Phys., 1 (1967), pp. 149–172.
[33] R. LI, Moving Mesh Method and its Application. PhD Thesis, Peking University, 2001. (in Chinese).
[34] R. LI AND W. B. LIU, `http://circus.math.pku.edu.cn/AFEPack`.
[35] B. NICENO, `http://www-dinma.univ.trieste.it/nirftc/research/easymesh`.
[36] P. WOODWARD AND P. COLELLA, *The numerical simulation of two-dimensional fluid flow with strong shocks*, J. Comput. Phys., 54(1) (1984), pp. 115–173.
[37] RALF DEITERDING, `http://amroc.sourceforge.net/`.